Article

Temperature-Dependent Sheet Resistance and Surface Characterization of Thin Copper Films Bonded to FR4 Composite under Mechanical Vibrations

Sufyan Azam [1,*], Shadi Munshi [1], Mohamed K. Hassan [1] and Alex Fragoso [2,*]

[1] Mechanical Engineering Department, Umm Al-Qura University, Makkah 21955, Saudi Arabia; smmunshi@uqu.edu.sa (S.M.); mkibrahiem@uqu.edu.sa (M.K.H.)
[2] Departament d'Enginyeria Química, Universitat Rovira i Virgili, 43007 Tarragona, Spain
* Correspondence: saazam@uqu.edu.sa (S.A.); alex.fragoso@urv.cat (A.F.)

Featured Application: Electrical and electronic devices that experience long-term vibrations.

Abstract: Electrical boards, also called printed circuit boards, constitute the basis of most electronic devices. These boards are mainly fabricated of thin copper films bonded to fiber epoxy laminates, such as FR4. Being the most important functional component of these devices, they sometimes undergo mechanical stresses such as shock and vibration during transport and operation that can induce electrical failure and malfunction; hence, studies addressing the effects of vibrations on their electrical properties have important applications. In this paper, small cantilever samples made of bare copper bonded to FR4 with three isolated rectangular zones were studied to analyze, for the first time, variations in electrical properties such as sheet resistance and resistivity before and after 200 k, 500 k, and 800 k vibration cycles at three different temperatures (25, 35, and 45 °C). A significant rise in resistance equivalent to 1657% of the initial value was observed from 0 to 800 k vibration cycles. These changes were accompanied by a 95% decrease in conductivity, from 4.1×10^7 to 2.3×10^6 S/m, whereas very little change in the electrical properties was observed due to temperature rise. Surface analysis by ESEM showed cracks ~1 µm in width and several millimeters in length with a crack density of ~8 cracks per mm after 800 k cycles. The surface composition (100% copper) was not altered even upon a high number of vibration cycles, and static drop contact angle measurements of 117–119 degrees indicated an increase in the hydrophobicity of the surface attributed to increased surface roughness and the accumulation of very small air bubbles on the cracks.

Keywords: copper/FR4 composite; printed circuit board; sheet resistance; vibrations; conductivity; resistivity; scanning electron microscope; hydrophilicity; X-ray diffraction

Citation: Azam, S.; Munshi, S.; Hassan, M.K.; Fragoso, A. Temperature-Dependent Sheet Resistance and Surface Characterization of Thin Copper Films Bonded to FR4 Composite under Mechanical Vibrations. *Appl. Sci.* **2023**, *13*, 7941. https://doi.org/10.3390/app13137941

Academic Editor: Andrea Li Bassi

Received: 22 June 2023
Revised: 2 July 2023
Accepted: 5 July 2023
Published: 6 July 2023

Copyright: © 2023 by the authors. Licensee MDPI, Basel, Switzerland. This article is an open access article distributed under the terms and conditions of the Creative Commons Attribution (CC BY) license (https://creativecommons.org/licenses/by/4.0/).

1. Introduction

Modern smart electronic devices consist of printed circuit boards (PCBs) and micro-electromechanical systems (MEMS) [1]. These devices are mainly fabricated using thin copper films bonded to fiber epoxy laminates and often contain a number of embedded components such as resistors, capacitors, etc. [2,3]. PCB board sizes have variable sizes (typically several centimeters) and are fabricated in multi-stage processes [4]. Their performance and reliability are often compromised by shock and vibration, which produce high stress loads on all parts of the device, including the substrate and its components [5,6].

The study of the interplay between the mechanical and electrical properties of thin films used in PCBs and MEMS is of great importance for evaluation of the performance and reliability of these devices. The physical and chemical properties of thin films vary from those of the bulk materials due to changes in anisotropy, porosity, and grain size, as well as the presence of surface oxide films [7–9], and they can be studied using a wide variety of performance tests and methods including stress relaxation, X-ray diffraction, indentation or

interferometry, among many others [10]. In an early work, Vinci and coworkers studied the effects of texture, thickness, and the passivation layer on the thermomechanical properties of thin copper films sputtered on a Si substrate [11]. Comparing mechanistic models with the measured properties, they found that oriented grains increased the stress between 15% and 22% in a thermal cycle compared with random orientations and, interestingly, passivation with silicon nitride induced a significant reduction in stress relaxation (~30%) at temperatures above 250 °C. Other studies have reported the mechanical properties of flexible [12–15] and rigid [16–19] copper films deposited on a variety of substrates to better understand their failure risk and durability [20,21]. For example, Park et al. [15] found that the elastic limit and ultimate tensile strength of Sn-coated Cu thin films, like those used in tape carrier packages, were 10 times and 2.5 times higher than those of copper bulk material, respectively. These properties are also influenced by temperature, as evidenced by Lee et al., who derived a modified Hall Petch equation to explain the decrease in stress with temperature and the microstructure of copper specimens electroplated with films containing oriented (200) and (220) planes [18]. The tensile and fatigue properties of copper thin films also depend on the processing method (rolling, electrolysis, direct current plating copper, and pulse plating), with rolled copper showing the highest resistance to crack initiation (~6 times slower crack propagation) compared with the other methods [22]. These results may be of importance in flexible electronics applications.

From a practical point of view, it is very important to investigate vibration fatigue damage (mechanical property) and its effect on the electrical resistance (functional property) of conductive thin films. Studies on the effects of high-cycle bending on the electrical properties of copper [23], indium-tin oxide [24], and other conductive films [25,26] have demonstrated that failure mechanisms should be accounted for during design steps to obtain robust and failure-free devices. To measure the electrical properties of thin wafers, such as sheet resistivity, the four-point probe is the most commonly used method [27]. Wenner [28] proposed this method in 1915 for the first time to measure Earth's resistivity. In 1954, Valdes [29] adopted this method to measure semi-conductor wafer resistivity. Usually probes are co-linear, i.e., arranged in-line with equal probe spacing; however, other configurations are also used in practice [28].

Here we present the influence of cyclic vibrations and temperature on the electrical properties of thin copper films bonded to FR4. A custom-made four-probe head was used to measure voltage and determine different electrical parameters such as sheet resistance, resistivity, and electrical conductivity at temperatures varying from 25 to 45 °C. The resulting film surface after fatigue loading was studied using scanning electron microscopy (SEM) and measuring the water droplet contact angle to better understand the relationship between damage accumulation and the electrical performance of PCB boards and MEMS.

2. Materials and Methods

2.1. Materials

The specimens used for measuring electrical properties such as sheet resistance, resistivity, and conductivity, were made of single-layer Cu film (thickness 18 µm) bonded to FR4 epoxy laminate sheet (thickness 1.5 mm). The specimens were cut from a 310 mm long and 210 mm wide panel to equal dimensions of 50 mm × 25 mm, using a Protomat S103 (LPKF GmbH, Garbsen, Germany) circuit board plotter. Three isolated rectangles (zones A, B, and C) with 10 mm × 5 mm dimensions were cut using a 0.1 mm micro cutter. The electrical properties of each rectangle were then measured separately using a custom-made dual-axes four-point probe (DA4PP). Figure 1 shows a photograph of the specimen with the actual dimensions and isolated rectangles. The line-shaded area represents the clamping side of the specimen to the rigid structure, while the blue-shaded area on the other side of the specimen represents the side linked to the shaker by means of a rigid steel rod on which the load cell was mounted.

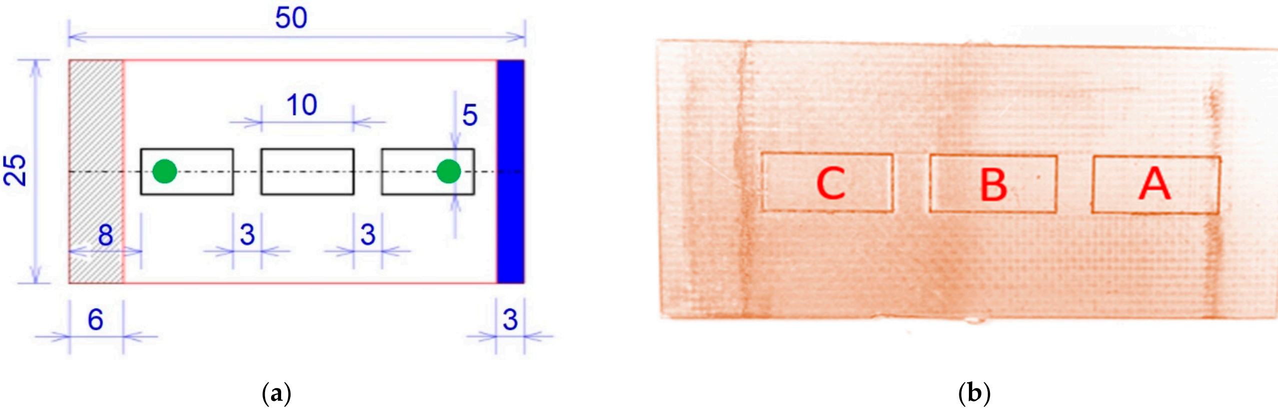

(a) (b)

Figure 1. Specimen details: (**a**) Dimensions (in mm): green filled circles represent sensor positions; (**b**) Actual photograph of the specimen with three isolated rectangles at positions A, B, and C.

The specimens were categorized into three sets and each set further consisted of three samples with three isolated rectangles on each sample, as shown in Table 1. The sample not subjected to any vibration was denoted S0.

Table 1. Specimen sets by temperature and number of cycles.

Specimen Set	Test Temperature (°C)	Number of Cycles
S11	25	200,000
S12	35	200,000
S13	45	200,000
S21	25	500,000
S22	35	500,000
S23	45	500,000
S31	25	800,000
S32	35	800,000
S33	45	800,000

2.2. Experimental Sheet Resistance Analysis

This experimental work was conducted in two stages. In the first stage, samples were subjected to mechanical vibrations for different numbers of cycles at a constant load of 30 N and sinusoidal frequency of 50 Hz. After achieving the required number of cycles, using a digital frequency counter, the samples were tested for sheet resistance at surface temperatures of 25, 35, and 45 °C, since this is the most common temperature interval at which electronic devices operate. The sheet resistance measurement setup consisted of two separate experimental setups. These are:

- DA4PP
- High Cycle Vibration Test Rig

2.2.1. DA4PP Design

Figure S1 shows a photograph of the DA4PP device. It consisted of a custom-made probe head having four in-line equally spaced probes and a temperature sensor, an auto mechanical stage, a source measure unit, a sample holding stage, and motion and communication software.

The probes were made of gold-plated tungsten metal with a 0.24 mm radius and equal spacing. The gold layer enabled good electrical contact with the copper surface. Each probe pin was supported by springs on the other end to minimize sample damage during probing. The probe head was part of the auto-mechanical stage, which traveled in two axes (up–down and left–right) to take measurements. A Keithley (Cleveland, OH, USA) model 2400 high impedance current source was used to supply current through the two outer

probes and measure the voltage across the two inner probes. The values of sourced current and measured voltage were used to determine the sample sheet resistance. Figure S2 shows a photograph of the wiring between the probe head and the Keithley 2400 source measure unit (SMU).

The probe spacing (S) was 1.27 mm. The probes exerted 60 g of force on the sample when fully pressed and had a stroke length of 1.4 mm. A J-type thermocouple was also part of the probe head to record the surface temperature of the specimen being tested. The surface temperature of the sample was recorded by an 8-channel thermocouple data logger type TC-08 (Pico Technology Ltd., St. Neots, UK)). The sample holding stage consisted of a silver plate that could be heated using two 100 W, 220 V silicon heaters (Keenovo International, Shanghai, China), which were installed at the bottom of the plate. The temperature of the inner plate surface was controlled by a PID temperature controller. The sample to be tested was placed at the top of the plate. Another part of the DA4PP device was the auto-mechanical stage. It consisted of two NEMA17 (Creality, Shenzhen, China) stepper motors for up–down and left–right movements of the probe head. The two motors were coupled with lead screws having 4 and 5 mm leads and 12 and 16 mm shaft diameters, respectively, as well as 1:80 step angle and 0.1 mm resolution. There were two inductive limit switches to determine the start position of the probe head. The probe head was installed on the vertical axis using an aluminum clamp with 32 mm internal diameter. A LabVIEW-based graphical user interface (GUI), as shown in Figure S3a, was designed to control the four-probe head movement. This GUI communicated with the motion controller, based on Arduino Mega microcontroller hardware, through a serial communication. Three levels of linear motion resolution could be achieved with this interface, namely 10, 1, and 0.1 mm. The home button brought the head to the reference position, and for sheet resistance measurement, an open source GUI was used, as shown in Figure S3b [30]. This GUI functioned with the Keithley 2400 SMU to perform current voltage characterization using the four-point probe. It communicated with the SMU through IEEE-488.2 GPIB communication protocol using a GPIB adapter. An I-V sweep, sourcing current and measuring voltage, was selected for the measurement of sheet resistance.

2.2.2. High Cycle Vibration Test Rig

The developed high cycle vibration design system consisted of the following elements: a signal generator, an amplifier, a digital frequency Counter, a vibration test rig, an FFT analyzer, and a PC with PULSE Labshop V8. Figure 2 shows the experimental layout for high cycle mechanical vibrations.

A signal generator module type 3107 (Brüel & Kjær, Virum, Denmark) was used to generate continuous sinusoidal signals at 50 Hz frequency rate. The parameters for the signal generator were set by PULSE Labshop V4.0. A digital frequency counter type 1805 (B&K Precision, Yorba Linda, CA, USA) counted the required number of cycles for the experiment and a power amplifier type 2706 (Brüel & Kjær) amplified the signals to be fed to the vibration exciter type 4809 (Brüel & Kjær). The vibration data were captured using a LAN XI type 3050-A-060 (Brüel & Kjær) hardware FFT analyzer. The data were then analyzed using PULSE LabShop V13.5.0 (Brüel & Kjær) to determine the vibration response of the transducers, i.e., an accelerometer and a load cell. The vibration exciter covered a wide range of frequencies (10~20 kHz) and a continuous peak-to-peak displacement of 8 mm and could impart 45 N sinusoidal force or up to 60 N with assisted cooling. A 75 VA Power Amplifier Type 2706 (Brüel & Kjær) was used to drive this vibration exciter. A load cell or force transducer type 8230 (Brüel & Kjær) was mounted above the shaker to recode the applied forces to the specimen. One side of the specimen was mounted on the rigid structure while the other end was connected to the load cell by means of a small clamping steel structure. An accelerometer type 4526 (Brüel & Kjær) was used to record the amplitudes of the vibrations at positions 1 and 2 (see Figure 3). Figure S4 shows a typical response of the force sensor both in the time and frequency domains.

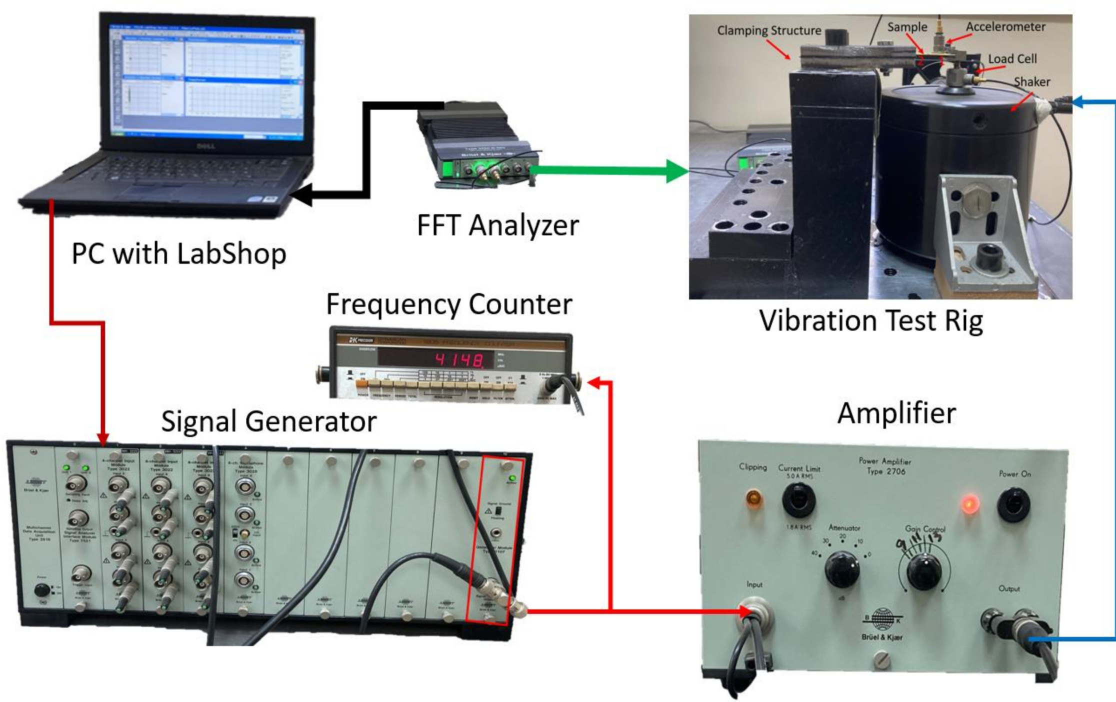

Figure 2. Experimental layout for high cycle mechanical vibrations.

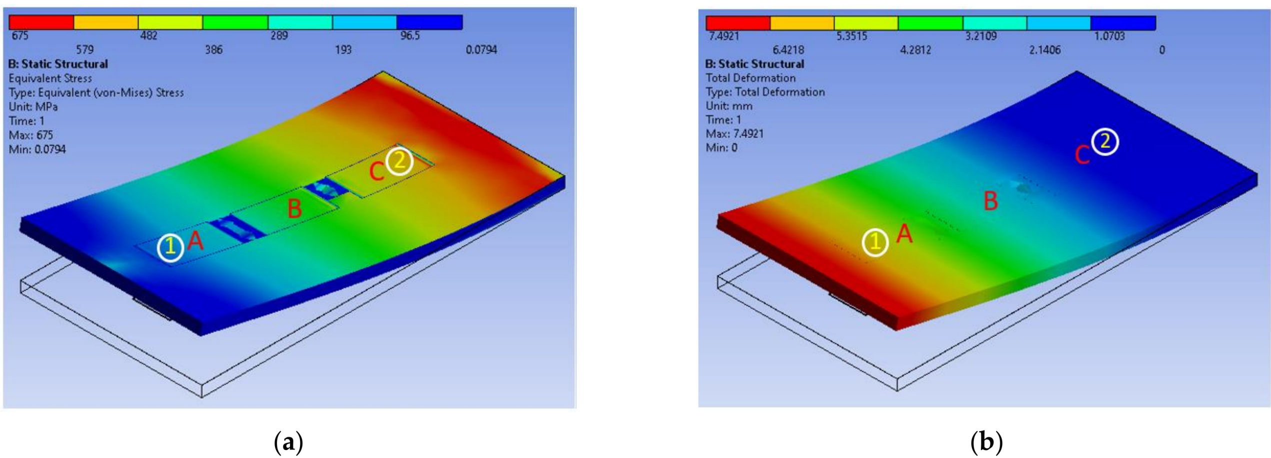

(**a**) (**b**)

Figure 3. Examples of specimen models used for FEM analysis: (**a**) Stress amplitude at positions 1 and 2; (**b**) Deformation at positions 1 and 2. Zones A, B, and C correspond to Figure 1.

A force amplitude of 30 N can be seen in the plot of Figure S4b. The higher amplitude at 50 Hz frequency confirmed the shaker input frequency of 50 Hz. The accelerometer response in the frequency domain at positions 1 and 2 can also be seen in Figure S5. Position 1, the free end of the cantilever, showed a very high amplitude of vibrations compared to position 2, the fixed end.

The vibration and stress amplitudes at positions 1 and 2 were modeled by FEM using ANSYSV19.3 workbench with Mechanical APDL solver using the fixed end (cantilever) as the boundary condition, as shown in Figure 3.

A mesh size of 1 mm of the shell element SOLSH190 was used for FEM modeling. The numbers of nodes and mesh elements were 26,895 and 4146, respectively. Both the FEM model in Figure 3a and accelerometer plot in Figure S5b showed less vibration amplitude but more stress amplitude at position 2.

2.3. Theoretical Model

A four-point probe setup, as shown in Figure 4, consisted of four equally spaced co-linear probes.

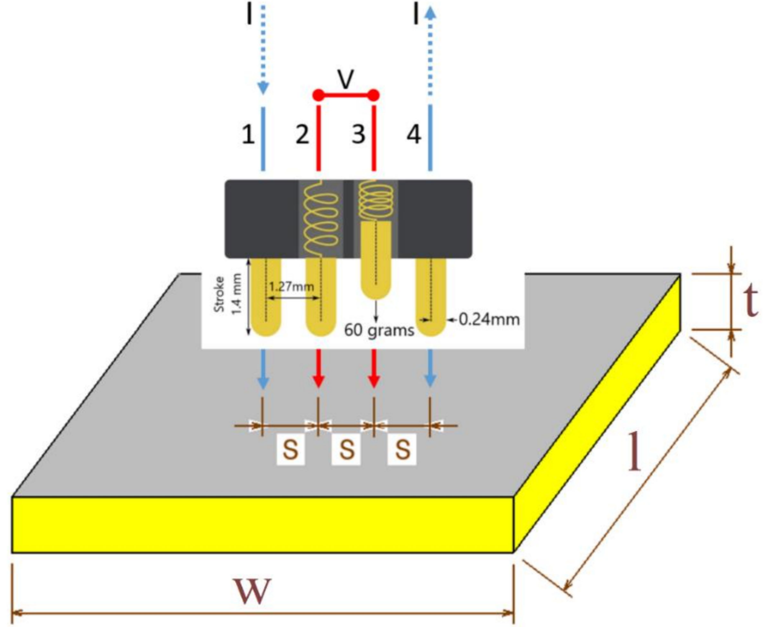

Figure 4. Schematic of the in line four-point probe setup indicating width (w), length (l), and thickness (t) of the specimen.

A small amount of DC current from a constant current source was applied through the two outer probes (1, 4) and the voltage drop was measured between the two inner probes (2, 3). The sheet resistance (R_{sh}) for a thin film with thickness t, where $t << w$ or l, is given by [28]:

$$R_{sh} = \frac{\pi}{\ln 2}\left(\frac{V}{I}\right) \approx 4.53\left(\frac{V}{I}\right)CF \quad [\Omega/sq], \tag{1}$$

where CF is the lateral correction factor for the probe, then the resistivity (ρ) in (Ohm-meter) is:

$$\rho = R_{sh}t \quad [\Omega m], \tag{2}$$

where t is the thin film thickness.

Similarly, electrical conductivity (σ), an intrinsic property of a material, is the measure of the amount of electrical current a material can carry or is able to carry. Electrical conductivity (Siemens per meter), also known as specific conductance, is the reciprocal of resistivity:

$$\sigma = \frac{1}{\rho} \quad [S/m], \tag{3}$$

2.4. Experimental Surface Analysis

The surface of the samples was examined using environmental scanning electron microscopy (ESEM) and contact angle measurements. ESEM images were recorded using a Quanta 600 microscope (FEI Company, Inc., Hillsboro, OR, USA) under high vacuum at 25 kV in the back-scatter mode. The samples were cleaned with a cloth soaked in acetone and dried under a nitrogen stream before analysis and probed at a 10 mm working distance at 50×, 500×, and 3000× magnification. The elemental composition was measured at 3000× magnification using the same instrument in XDS mode.

The contact angles were measured at different locations on the samples, as shown in Figure 5.

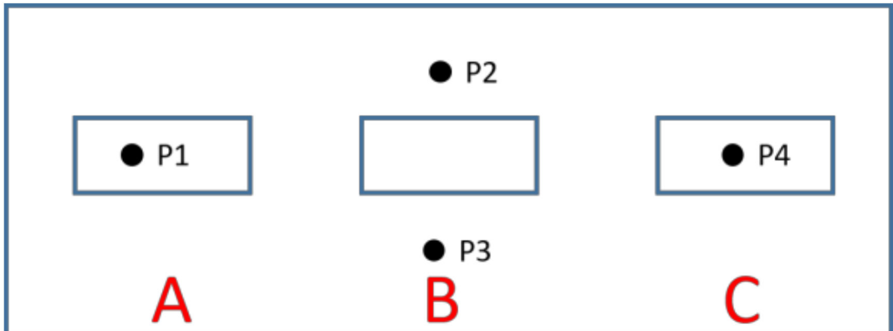

Figure 5. Water droplet locations for contact angle measurements. Zones A, B, and C correspond to Figure 1.

The static drop method using an OCA 15 plus goniometer (Neurtek Instruments, Eibar, Spain) with an image resolution of 752 × 582 pixels and ±0.1° accuracy was used for this test. The drop volume was 10 µL, and measurements were performed at a controlled temperature of 24 °C and ambient humidity of 55%.

3. Results

3.1. Validation and Repeatability

In order to validate the device performance, a set of ITO samples consisting of OSSILA glass substrate coated with a 100 nm layer of indium tin oxide (ITO) [31] were validated using the DA4PP. The reference sample had dimensions of 20 × 15 mm with a sheet resistance of 14–16 Ω/sq. The measurement results were then compared to the results obtained with the commercially available Ossila Four-Point Probe System [31]. The obtained results were in good agreement, as shown in Figure S6.

The average sheet resistance value (R_{sh}) obtained by the DA4PP was 14.75 Ω/sq, as compared with the Ossila reference sample value of 14.36 Ω/sq. The comparison between the theoretical (calculated) and measured resistance can be seen in Table 2. The theoretical calculations were performed using the following equation for resistance with a temperature coefficient at 20 °C [32]:

$$\mathrm{R} = \rho_{20}\frac{L}{\mathrm{tW}}[1+\alpha(T_{20}-T)][\Omega], \quad (4)$$

where ρ_{20} is the copper resistivity at 20 °C (1.67 × 10^{-8} Ωm), L is the length of the copper trace in mm, W is the width of the copper trace in mm, t is the thickness of the copper trace in µm, and α is the temperature coefficient at 20 °C (3.93 × 10^{-3} °C^{-1}). The measurement results showed a good correlation at 45 °C, with 4.21% discrepancy. The maximum difference in the results of 7.46% was obtained at 25 °C.

Table 2. Comparison of the theoretical and experimental resistance values.

Resistance (Ω)						
Temperature	**Length**	**Width**	**Thickness**	**R_{th} [1]**	**R_{exp} [2]**	**Difference**
(°C)	**(mm)**	**(mm)**	**(µm)**	**(Ω)**	**(Ω)**	**%**
25				4.638 × 10^{-4}	4.317 × 10^{-4}	7.46
35	5	10	18	4.821 × 10^{-4}	4.559 × 10^{-4}	5.74
45				5.003 × 10^{-4}	4.801 × 10^{-4}	4.21

[1] R_{th}: Theoretical resistance; [2] R_{exp}: Experimental resistance.

The performance of the DA4PP was quantified by measuring the resistance values of different samples at different temperatures and mechanical vibration cycles and finding the standard deviation (SD) and coefficient of variation (CV). Table 3 shows the resistance values at varying input parameters for the three measurement zones. The maximum

variation in the data values was in zone B at 800 k cycles and 45 °C. The coefficient of variation for this zone was 3.25%. Interestingly, similar behavior could be seen in other cases for zone B.

Table 3. Resistance variations before and after 800 k cyclic loading at 25 and 45 °C.

Replicate [1]	Zone A			Zone B			Zone C		
	Resistance (Ω)	SD [2] (Ω)	CV [3] (%)	Resistance (Ω)	SD [2] (Ω)	CV [3] (%)	Resistance (Ω)	SD [2] (Ω)	CV [3] (%)
Before cycling at 25 °C									
I	4.218×10^{-4}			4.233×10^{-4}			4.589×10^{-4}		
II	4.207×10^{-4}	2.44×10^{-6}	0.58	4.151×10^{-4}	3.92×10^{-6}	0.94	4.591×10^{-4}	1.03×10^{-6}	0.22
III	4.161×10^{-4}			4.149×10^{-4}			4.568×10^{-4}		
After 800 k cycles of loading at 25 °C									
I	1.906×10^{-3}			1.961×10^{-3}			3.432×10^{-2}		
II	1.904×10^{-3}	1.09×10^{-5}	0.57	1.904×10^{-3}	5.45×10^{-5}	2.87	3.434×10^{-2}	6.02×10^{-5}	0.17
III	1.882×10^{-3}			1.828×10^{-3}			3.421×10^{-2}		
Before cycling at 45 °C									
I	4.636×10^{-4}			4.744×10^{-4}			4.653×10^{-4}		
II	4.623×10^{-4}	4.42×10^{-6}	0.96	4.554×10^{-4}	8.50×10^{-6}	1.84	4.520×10^{-4}	5.58×10^{-6}	1.22
III	4.536×10^{-4}			4.576×10^{-4}			4.562×10^{-4}		
After 800 k cycles of loading at 45 °C									
I	2.091×10^{-3}			2.153×10^{-3}			3.543×10^{-2}		
II	2.110×10^{-3}	1.23×10^{-5}	0.58	2.063×10^{-3}	6.72×10^{-5}	3.25	3.668×10^{-2}	8.29×10^{-4}	2.27
III	2.121×10^{-3}			1.989×10^{-3}			3.745×10^{-2}		

[1] Measurements performed in three identical replicates; [2] SD: standard deviation; [3] CV: coefficient of variation.

The above-mentioned results indicated that the custom-made DA4PP showed very good repeatability and accurately measured the sample resistance in all regions, so it could be used to measure resistance changes after mechanical vibrations and thermal loading.

3.2. Electrical Properties under Mechanical Vibrations at Different Temperatures

3.2.1. Resistance

In general, the four-point probe method is used to determine the sheet resistance of thin metal films, but in fact, resistance is the main electrical property assessed using this technique. In a four-point probe, the outer probes apply current to the sample and the inner probes measure voltage. The slope of the I-V curve then gives the resistance value for the sample being tested. Figures 6–8 show the resistance plots with respect to time at 25, 35, and 45 °C, respectively. The start of the measurement shows a high value of resistance, because contact resistance exists between the probe and sample, and a large current must flow through the sample so that the voltage generated between the inner two probes will be large enough to be accurately measured [33]. Hence, the resistance values were taken at the end of the measurement (3 s after the start).

It was observed that the stress amplitude was higher near measurement zone C as compared to the other two zones i.e., zones A and B (see Figure 3a). The number of vibration cycles played a significant role in changing the resistance values of zone C because of the stresses near this zone. The resistance variations due to temperature rise were very little in all of the above figures. Figure 9 shows 3D bar plots of the average resistance values, obtained from the I-V curves, against the number of vibration cycles and at different temperatures.

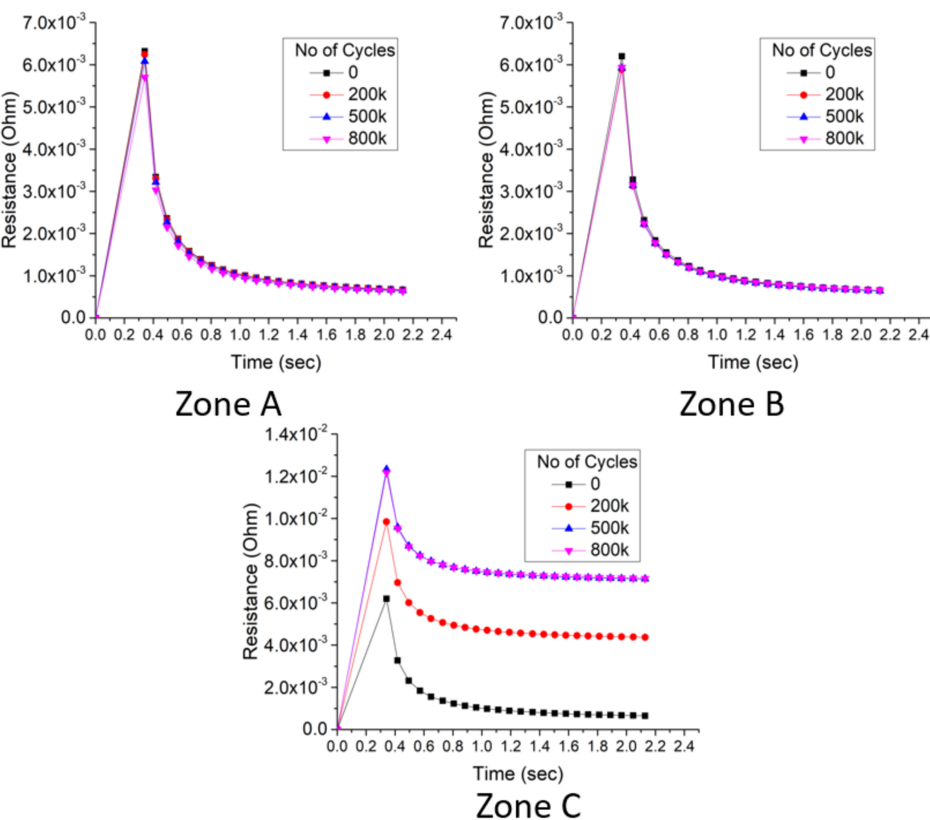

Figure 6. Plot of resistance vs. time under 0, 200 k, 500 k, and 800 k cycles at 25 °C. The measurements were performed using the setups depicted in Figures 2 and 4.

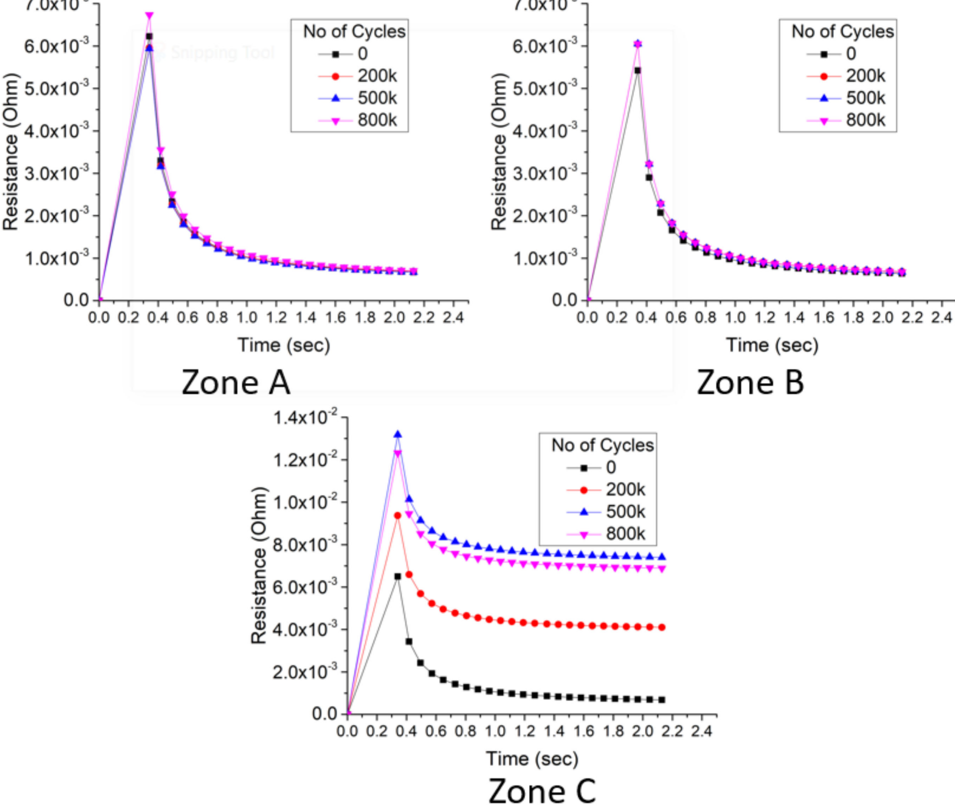

Figure 7. Plot of resistance vs. time under 0, 200 k, 500 k, and 800 k cycles at 35 °C. The measurements were performed using the setups depicted in Figures 2 and 4.

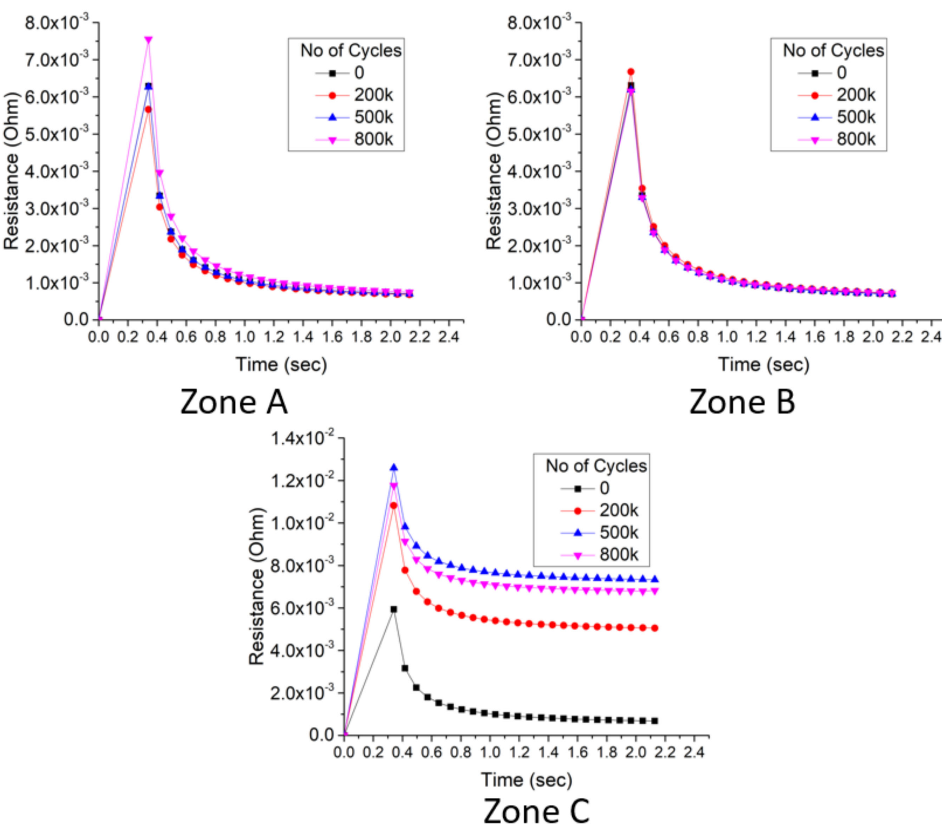

Figure 8. Plot of resistance vs. time under 0, 200 k, 500 k, and 800 k cycles at 45 °C. The measurements were performed using the setups depicted in Figures 2 and 4.

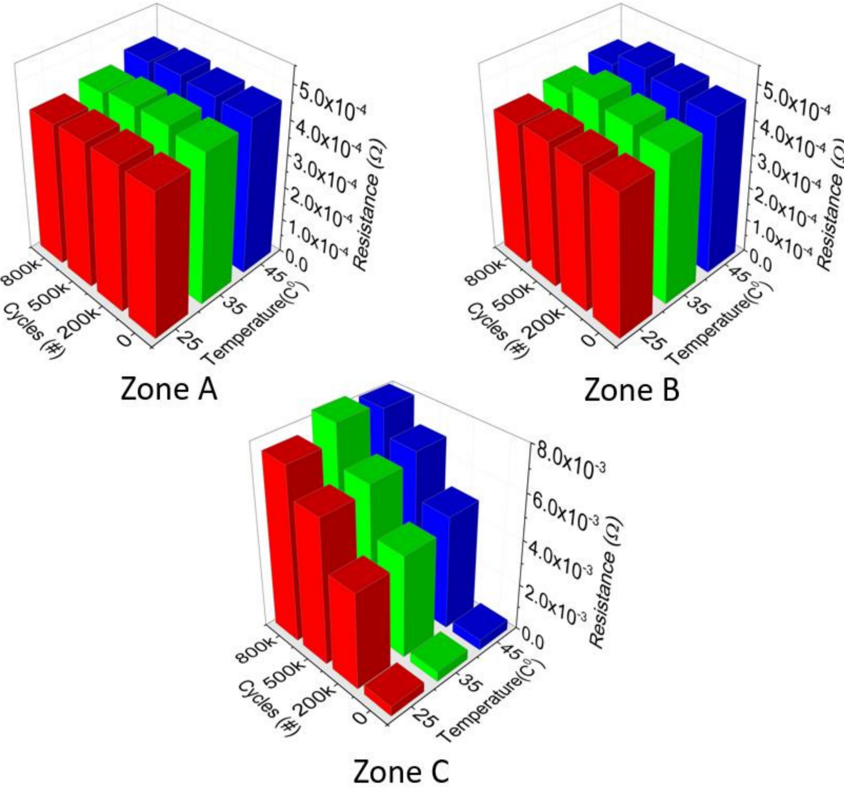

Figure 9. 3D bar plot of resistance against number of mechanical cycles and temperature.

An exponential rise in resistance could be seen due to the number of vibration cycles whereas very little change was observed due to the temperature rise. There was a 1657% rise in resistance values from 0 cycles to 800 k cycles at 45 °C for zone C, whereas this change was very little for zones A and B, around 1.1% and 1.34%, respectively.

3.2.2. Sheet Resistance, Resistivity, and Conductivity

The average sheet resistance values plotted against the number of vibration cycles and at different temperatures can be seen in Figure 10.

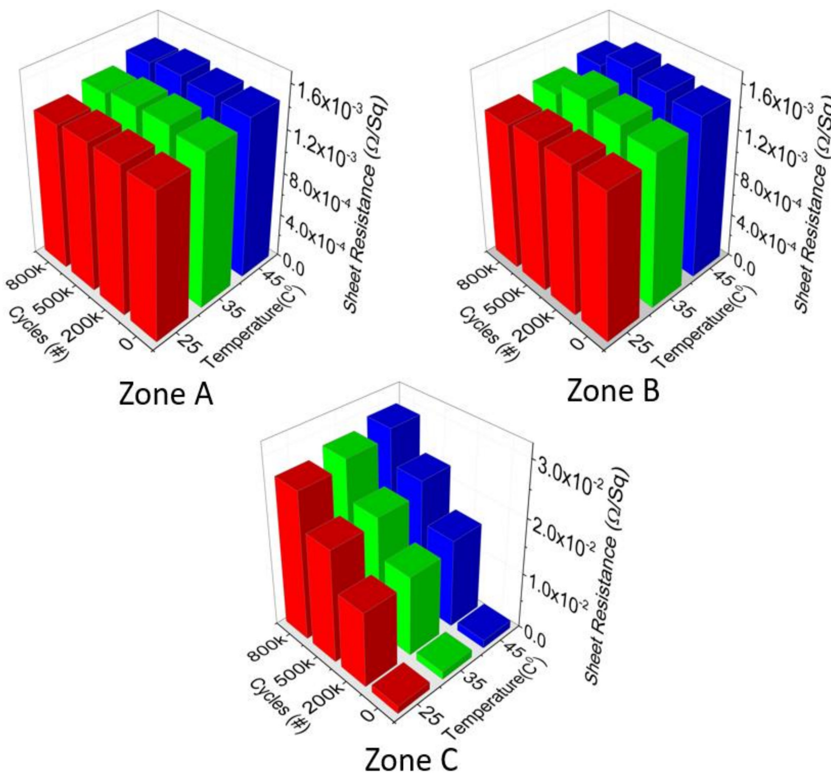

Figure 10. 3D bar plot of sheet resistance against number of mechanical cycles and temperature.

As opposed to resistance, sheet resistance can directly be measured using four-point probe measurements. The effect of the mechanical cycles on zone C could be clearly observed with an exponential rise in sheet resistance values. Before cyclic loading at 25 °C, the sheet resistance values for zones A, B, and C were 1.34, 1.33, and 1.33 mΩ/sq, respectively. When the same sample was subjected to 800 k cycles, the sheet resistance values at 25 °C for zones A, B, and C were 1.34, 1.33, and 24.19 mΩ/sq, respectively. This behavior was not seen in the case of thermal loading, where a 20 °C rise in temperature gave only a 1% rise in average sheet resistance value. All of the zones behaved in a similar way under thermal loading.

The next two electrical properties obtained from the experimental work were resistivity (ρ) and conductivity (σ), as shown in Figures 11 and 12, respectively. Resistivity is the inherent property of the material that quantifies the strength of the material to resist or conduct electric current. As seen in the previous Figures 9 and 10, the mechanical vibration cycles played an important role in changing the electrical properties of the sample being tested, which also applied to resistivity and conductivity. After the sample underwent 800 k cycles, zone C of the sample became more resistive and the value of resistivity changed from 2.40×10^{-8} to 4.35×10^{-7} Ω.m. On the other hand, zones A and B still showed almost same values even after nearly a million cycles.

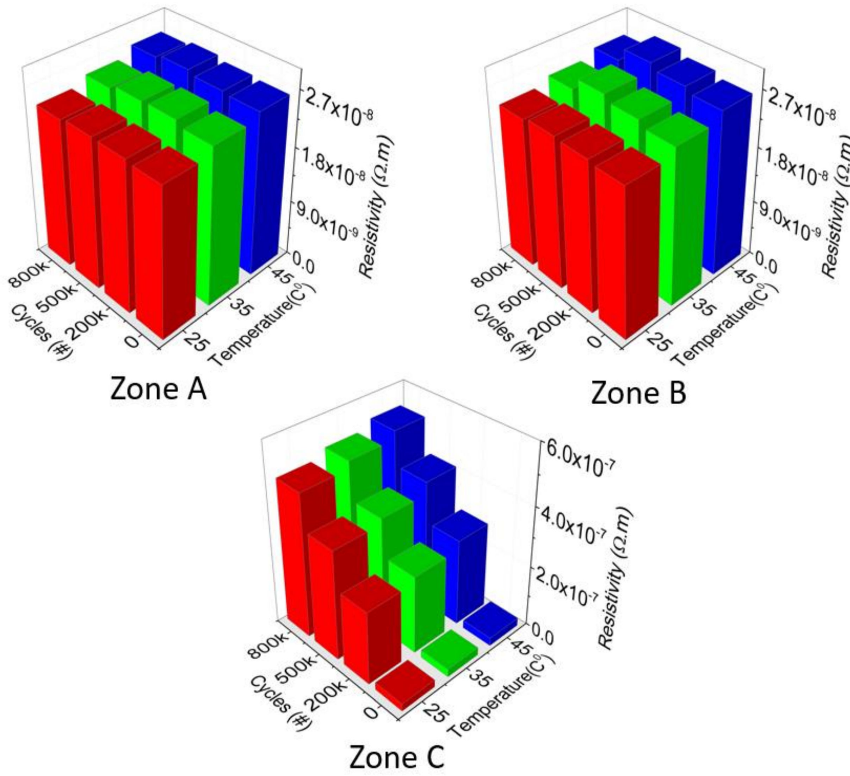

Figure 11. 3D bar plot of resistivity against number of mechanical cycles and temperature.

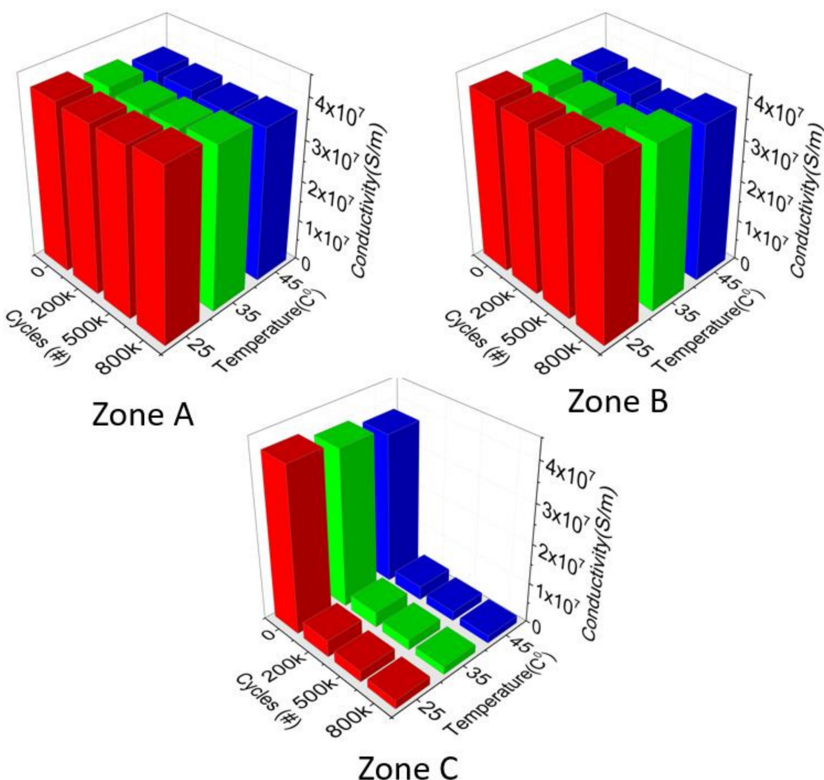

Figure 12. 3D bar plot of conductivity against number of mechanical cycles and temperature.

The last electrical property to study was conductivity (σ). Being the reciprocal of resistivity, conductivity quantifies how smoothly current flows in a conductor. A large value of σ means the material is a very good conductor of electrical current. Figure 12

shows the average conductivity values measured for the different zones under different numbers of vibration cycles and temperatures. Almost a 95% decrease in conductivity, from 4.15×10^7 to 2.29×10^6 S/m, could be observed after 800 k cycles for zone C. Slight variations due to temperature could also be seen in all three zones.

The large variations in the electrical properties of the samples after mechanical cyclic loading near zone C were due to the large amplitudes of the stresses near this area. This great change in the electrical properties led to surface analysis to better understand the microstructural changes in zone C that propagated the electrical changes in the samples.

3.3. Surface Analysis

Vibration stress produced a noticeable change in the surface color of all samples. The typical lustrous reddish-brown color of undamaged copper changed to dark brown after vibrations, indicating damage and/or chemical modification (i.e., oxidation) to the surface. For these reasons, the samples were analyzed by ESEM, elemental composition, and contact angle measurements.

Figures 13–15 show ESEM pictures of samples S0, S11, and S31 at 50×, 500×, and 3000× magnification, respectively. The morphology of the untreated sample showed a smooth surface without cracks at 50× (Figure 13a) and the presence of rolling traces of crystalline domains was probably due to the mode of fabrication of the samples (Figures 14a and 15a).

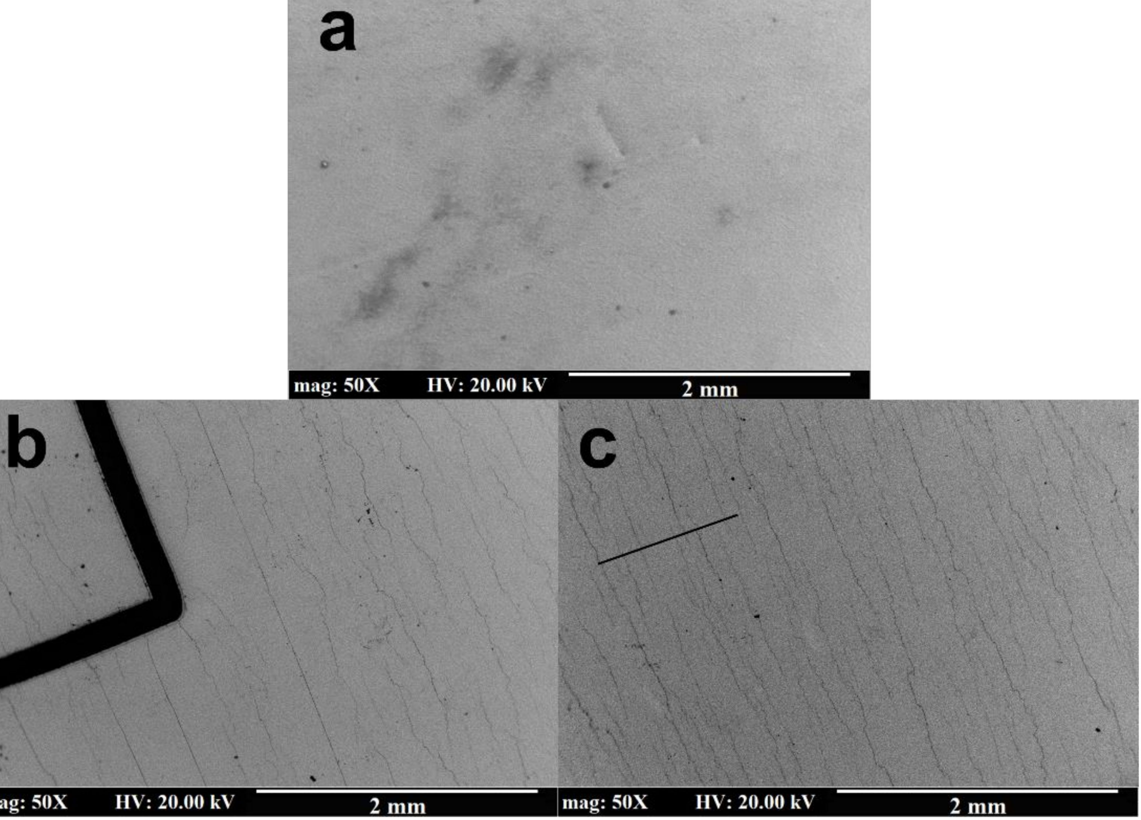

Figure 13. ESEM images (back-scatter mode) of samples S0 (**a**), S11 (**b**), and S31 (**c**) at 50× magnification.

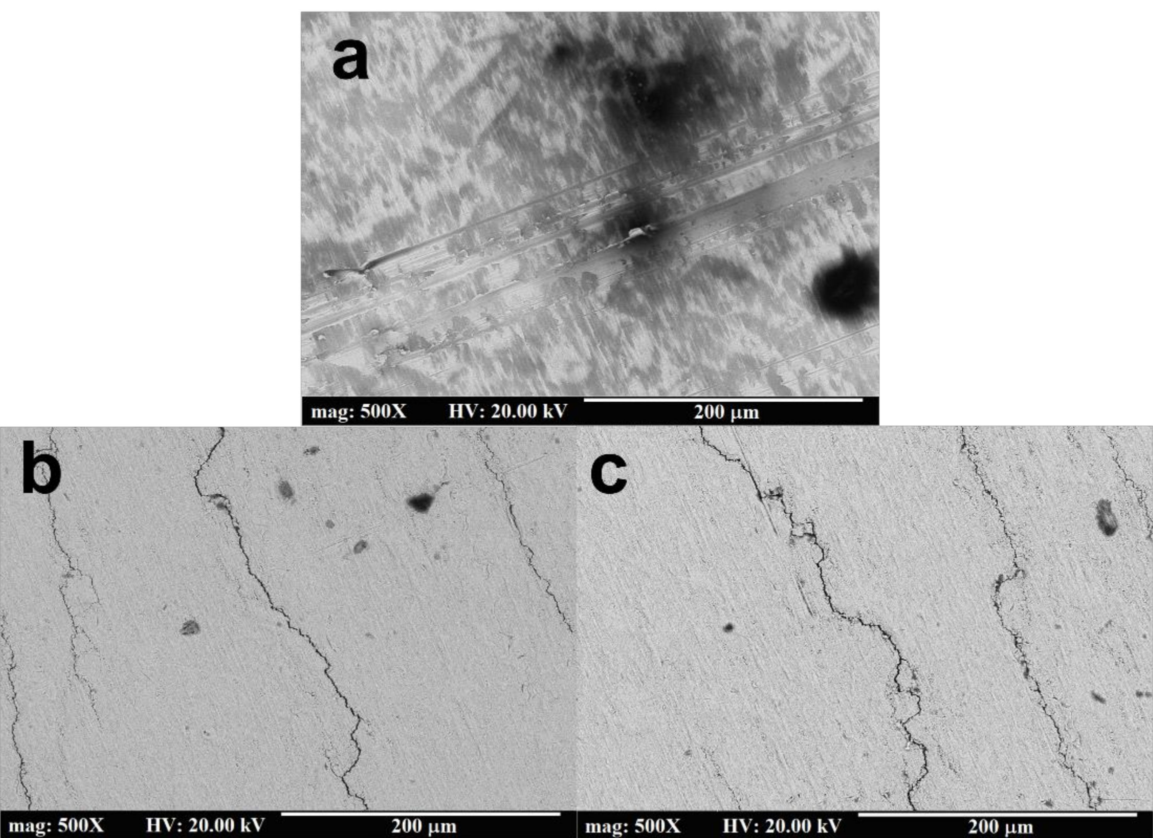

Figure 14. ESEM images (back-scatter mode) of samples S0 (**a**), S11 (**b**), and S31 (**c**) at 500× magnification.

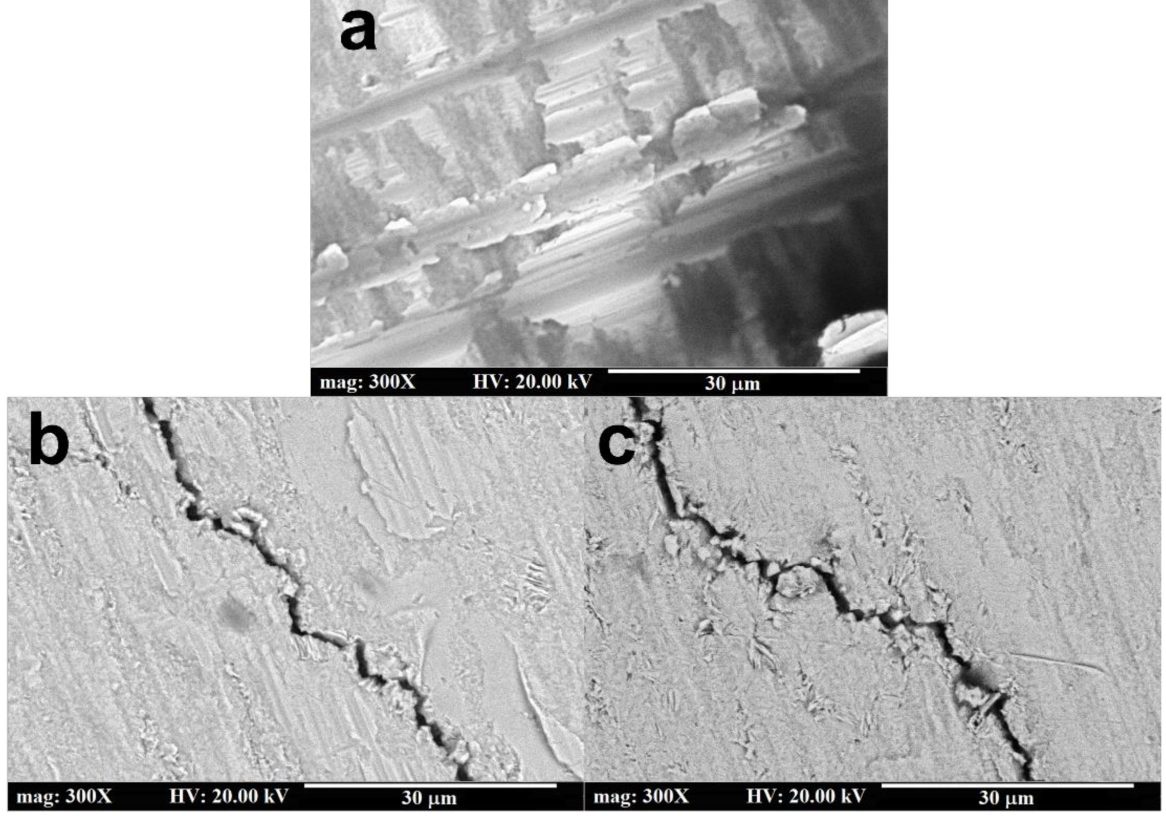

Figure 15. ESEM images (back-scatter mode) of samples S0 (**a**), S11 (**b**), and S31 (**c**) at 3000× magnification.

After 200 k and 800 k vibration cycles, the surfaces clearly developed cracks, as evidenced in panels (b) and (c) of Figures 13–15. These cracks were perpendicular to the longitudinal axis of the samples and were the result of the plastic deformation undergone by the samples after vibration stress. The apparent density of cracks increased with the number of cycles from ~3 cracks per mm at 200 k cycles to ~8 cracks per mm at 800 k cycles, indicating a dependence of the overall damage on the number of cycles. These cracks were ~1 µm in width and several millimeters in length and seemed to follow dislocation lines perpendicular to the longitudinal axis, as shown in Figure 16.

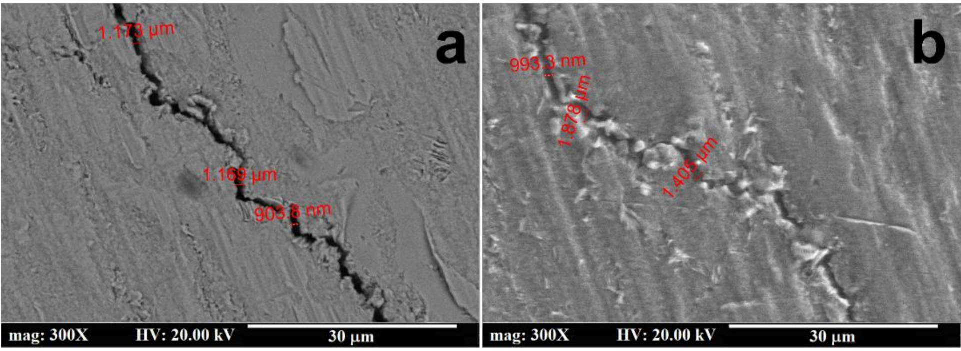

Figure 16. ESEM images corresponding to Figure 15b,c, respectively, showing crack dimensions (at 3000× magnification).

This type of crack development has been observed in other fatigue studies of copper thin films and is attributed to the presence of dislocations [34,35] and favored by surface roughness [36].

Interestingly, the surface composition (100% copper) was not altered even upon a high number of vibration cycles, indicating that the vibration stress only produced physical damage and not chemical processes such as oxidation, as shown in Figure 17. The samples were also analyzed by measuring the water droplet contact angle. This technique is useful in assessing hydrophilicity/hydrophobicity changes on surfaces and is widely used in adsorption and surface modification studies [37]. Figures 18 and 19 show the contact angle measurements for samples before and after vibrations, respectively.

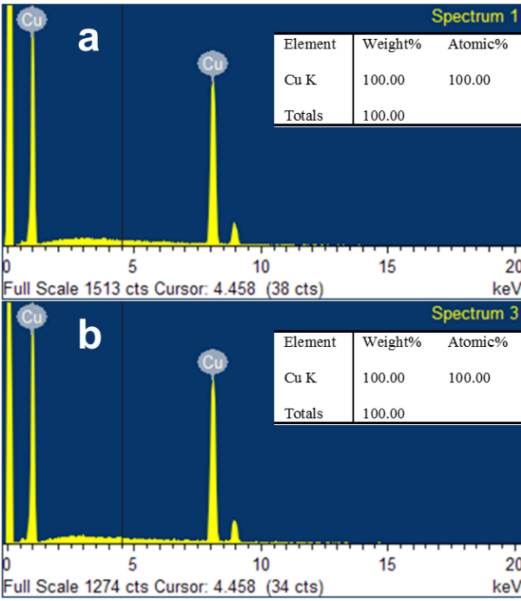

Figure 17. Surface elemental composition of samples corresponding to: (**a**) Figure 14a (before vibrations); (**b**) Figure 14c (after vibrations).

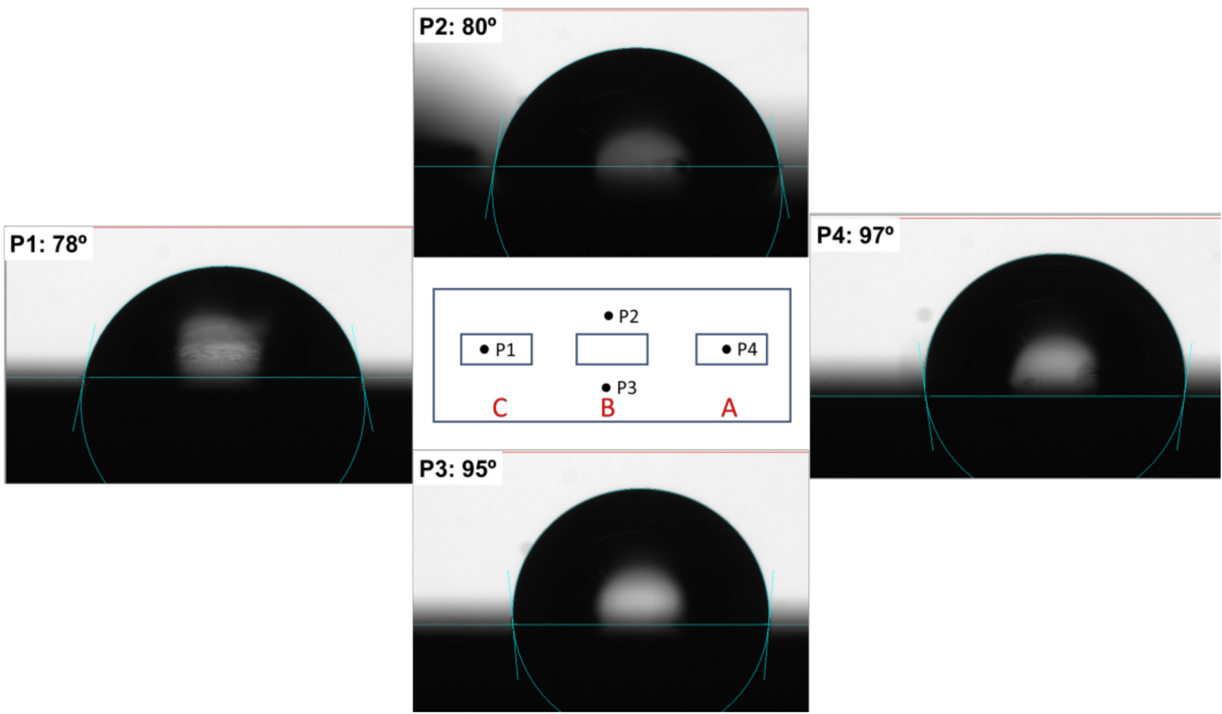

Figure 18. Contact angle measurements of sample S0 at different locations. Zones A, B, and C correspond to Figure 1.

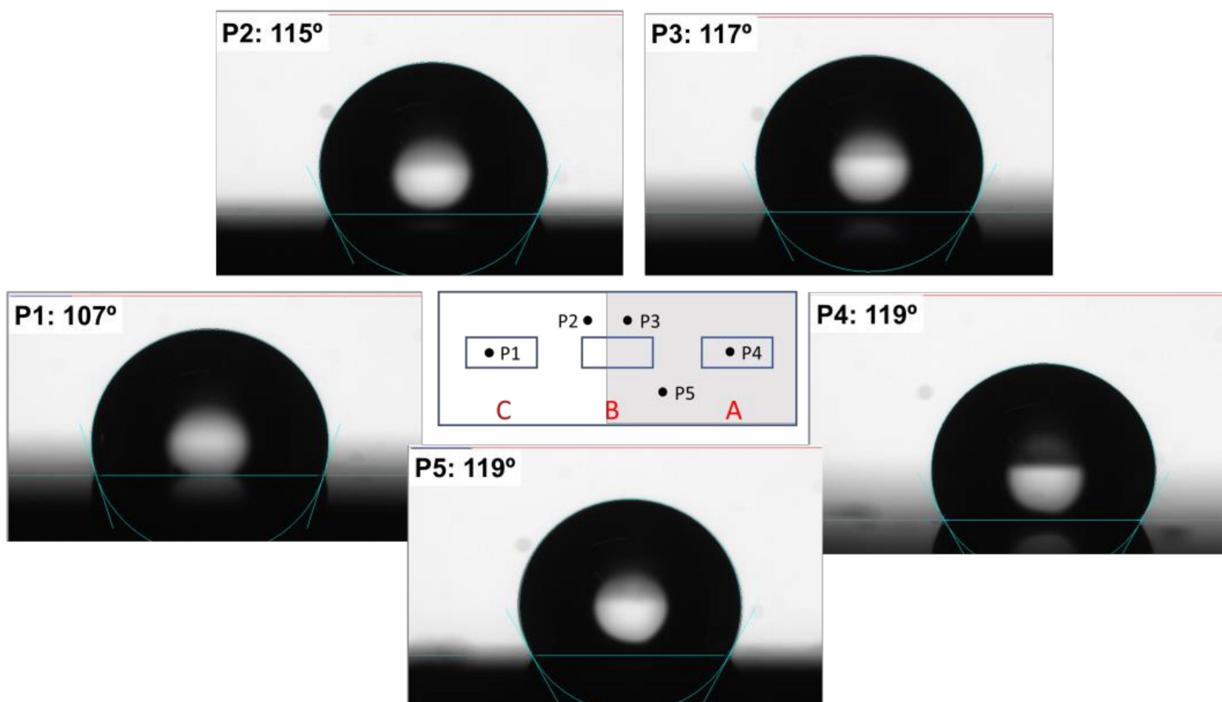

Figure 19. Contact angle measurements of sample S31 at different locations. The grey area indicates a higher density of cracks in the sample. Zones A, B, and C correspond to Figure 1.

The observed contact angles for untreated samples ranged from 78 to 95 degrees, similar to those observed for pure copper, indicating a hydrophilicity similar to that of aluminum [38]. After vibration damage, the contact angle increased to 117–119 degrees, typical of a hydrophobic surface such as PTFE (polytetrafluoroethylene). This marked change in contact angle could be attributed to increased surface roughness [39] and also to

the accumulation of very small air bubbles on the cracks that hindered water contact with the surface.

4. Conclusions

The effects of mechanical vibrations and thermal variations on the electrical properties of thin copper films of 18 µm thickness bonded to FR4 epoxy laminate of 1.5 mm thickness were determined experimentally for the first time. It was evident from the results obtained at zone C that the stress induced by mechanical vibrations plays an important role in the electrical properties of PCBs. Resistance values increased up to 1657% of the initial value after 800 k vibration cycles. These changes were associated with a 95% decrease in conductivity (from 4.1×10^7 to 2.3×10^6 S/m). This was due to the surface damage caused by mechanical vibrations near this zone. Interestingly, no such behavior was observed at zones A and B. At these zones, the electrical properties of the samples before and after mechanical vibration cycles were almost the same. No cracks were found near these zones, whereas the apparent density of cracks at zone C, as seen by ESEM, increased from ~3 cracks per mm at 200 k cycles to ~8 cracks per mm at 800 k cycles. This indicated the dependence of the overall damage on the number of cycles. Interestingly, very little change in the electrical properties was observed due to temperature rise.

The surface composition analysis indicated that vibration stress only produced physical damage and not chemical processes such as oxidation. The samples were also analyzed using water droplet contact angle measurements. The observed contact angles for untreated samples (78 to 95 degrees) were found to be lower than those after mechanical vibrations (117–119 degrees). This marked change in contact angle could be attributed to increased surface roughness and the accumulation of very small air bubbles on the cracks, which made water contact with the surface difficult. Further studies will also address the influence of film thickness, material, and vibration frequency on the electrical performance of these composites under mechanical vibrations.

Supplementary Materials: The following supporting information can be downloaded at: https://www.mdpi.com/article/10.3390/app13137941/s1. Figure S1: Photograph of the dual axes four point probe (DA4PP) device. Figure S2: Photograph of the wring between probe head and keithley2400 source measure unit. Figure S3: Screenshot of the GUI: (a) For probe head movement; (b) For sheet resistance measurement. Figure S4: Plot of the force sensor: (a) In the time domain; (b) In the frequency domain. Figure S5: Frequency response of the accelerometer: (a) At position (1); (b) At position (2). Figure S6: Comparison of the sheet resistance values measured by two devices.

Author Contributions: S.A. conceptualization, methodology, investigation, data curation, writing—original draft preparation; M.K.H. conceptualization, validation; S.M. methodology, project administration, funding acquisition; A.F. conceptualization, writing—review and editing, supervision. All authors have read and agreed to the published version of the manuscript.

Funding: This work has been funded by the Deanship of Scientific Research at Umm Al-Qura University. Grant code: 23UQU4330020DSR01.

Institutional Review Board Statement: Not applicable.

Informed Consent Statement: Not applicable.

Data Availability Statement: All data are included I the text.

Acknowledgments: The authors would like to thank the Deanship of Scientific Research at Umm Al-Qura University for supporting this work under grant 23UQU4330020DSR01.

Conflicts of Interest: The authors declare no conflict of interest.

References

1. Canal Marques, A.; Cabrera, J.-M.; de Fraga Malfatti, C. Printed circuit boards: A review on the perspective of sustainability. *J. Environ. Manag.* **2013**, *131*, 298–306. [CrossRef] [PubMed]
2. Sankar, V.U.; Lakshmi, G.; Sankar, Y.S. A Review of Various Defects in PCB. *J. Electron. Test.* **2022**, *38*, 481–491. [CrossRef]

3. Jillek, W.; Yung, W.K.C. Embedded components in printed circuit boards: A processing technology review. *Int. J. Adv. Manuf. Technol.* **2005**, *25*, 350–360. [CrossRef]
4. LaDou, J. Printed circuit board industry. *Int. J. Hyg. Environ. Health* **2006**, *209*, 211–219. [CrossRef] [PubMed]
5. Zhou, S.; Lin, Z.; Qiu, B.; Wang, H.; Xiong, J.; He, C.; Zhou, B.; Pan, Y.; Huang, R.; Bao, Y.; et al. Evaluation of Solder Joint Reliability in 3D Packaging Memory Devices under Thermal Shock. *Electronics* **2022**, *11*, 2556. [CrossRef]
6. Jiao, J.; De, X.; Chen, Z.; Zhao, T. Integrated circuit failure analysis and reliability prediction based on physics of failure. *Eng. Fail. Anal.* **2019**, *104*, 714–726. [CrossRef]
7. Connolley, T.; McHugh, P.E.; Bruzzi, M. A review of deformation and fatigue of metals at small size scales. *Fatigue Fract. Eng. Mater. Struct.* **2005**, *28*, 1119–1152. [CrossRef]
8. O'Reilly, M.; Jiang, X.; Beechinor, J.T.; Lynch, S.; NíDheasuna, C.; Patterson, J.C.; Crean, G.M. Investigation of the oxidation behaviour of thin film and bulk copper. *Appl. Surf. Sci.* **1995**, *91*, 152–156. [CrossRef]
9. Baker-Jarvis, J.; Jones, C.A. Dielectric Measurements on Printed-Wiring And Circuit Boards, Thin Films, And Substrates: An Overview. *MRS Online Proc. Libr.* **1995**, *381*, 153–164. [CrossRef]
10. Gunda, M.; Kumar, P.; Katiyar, M. Review of Mechanical Characterization Techniques for Thin Films Used in Flexible Electronics. *Crit. Rev. Solid State Mater. Sci.* **2017**, *42*, 129–152. [CrossRef]
11. Vinci, R.P.; Zielinski, E.M.; Bravman, J.C. Thermal strain and stress in copper thin films. *Thin Solid Films* **1995**, *262*, 142–153. [CrossRef]
12. Girard, G.; Martiny, M.; Mercier, S. Experimental characterization of rolled annealed copper film used in flexible printed circuit boards: Identification of the elastic-plastic and low-cycle fatigue behaviors. *Microelectron. Reliab.* **2020**, *115*, 113976. [CrossRef]
13. Fellner, K.; Fuchs, P.F.; Pinter, G.; Antretter, T.; Krivec, T. Method development for the cyclic characterization of thin copper layers for PCB applications. *Circuit World* **2014**, *40*, 53–60. [CrossRef]
14. Park, J.H.; An, J.H.; Kim, Y.J.; Huh, Y.H.; Lee, H.J. Tensile and high cycle fatigue test of copper thin film. *Mater. Werkst.* **2008**, *39*, 187–192. [CrossRef]
15. Han, S.W.; Seo, K.J.; Kim, W.D.; Lee, H.J.; Lee, H.W.; Shin, J.H.; Lee, J.J. Fatigue Behavior of Thin Cu Foils for Flexible Printed Circuit Board. *Solid State Phenom.* **2007**, *124–126*, 1369–1372. [CrossRef]
16. Shin, H.-K.; Kim, S.-H.; Park, H.; Lee, H.-J. Multilayer Laminated Copper Electrodeposits and Their Mechanical Properties. *J. Electrochem. Soc.* **2022**, *169*, 102502. [CrossRef]
17. Trost, C.O.W.; Wurster, S.; Freitag, C.; Steinberger, A.; Cordill, M.J. A new approach to evaluate the elastic modulus of metallic foils. *Mater. Des.* **2020**, *196*, 109149. [CrossRef]
18. Lee, Y.-S.; Ha, S.; Park, J.-H.; Lee, S.-B. Structure-dependent mechanical behavior of copper thin films. *Mater. Charact.* **2017**, *128*, 68–74. [CrossRef]
19. Walter, T.; Khatibi, G.; Nelhiebel, M.; Heinz, W.; Robl, W. High cycle fatigue properties of Cu films. *Microelectron. Eng.* **2015**, *137*, 64–69. [CrossRef]
20. Menon, S.; Chen, D.Y.; Osterman, M.; Pecht, M.G. Copper Trace Fatigue Life Modeling for Rigid Electronic Assemblies. *IEEE Trans. Device Mater. Reliab.* **2021**, *21*, 79–86. [CrossRef]
21. Zhang, S.; Sakane, M.; Nagasawa, T.; Kobayashi, K. Mechanical Properties of Copper Thin Films Used in Electronic Devices. *Procedia Eng.* **2011**, *10*, 1497–1502. [CrossRef]
22. Min, H.-G.; Kang, D.-J.; Park, J.-H. Comparison of Tensile and Fatigue Properties of Copper Thin Film Depending on Process Method. *Appl. Sci.* **2020**, *10*, 388. [CrossRef]
23. Vandevelde, B.; Willems, G. Early fatigue failures in copper wire bonds inside packages with low CTE green mold compounds. In Proceedings of the 2012 4th Electronic System-Integration Technology Conference, Amsterdam, The Netherlands, 17–20 September 2012; pp. 1–4.
24. Alzoubi, K.; Hamasha, M.M.; Lu, S.; Sammakia, B. Bending Fatigue Study of Sputtered ITO on Flexible Substrate. *J. Disp. Technol.* **2011**, *7*, 593–600. [CrossRef]
25. Su, B.; Qu, J. Fatigue Behavior of Electrically Conductive Adhesives. *J. Adhes. Sci. Technol.* **2008**, *22*, 927–946. [CrossRef]
26. Kim, H.; Park, M.; Hsieh, K. Fatigue fracture of embedded copper conductors in multifunctional composite structures. *Compos. Sci. Technol.* **2006**, *66*, 1010–1021. [CrossRef]
27. Simon, M.; Sze, K.K.N. *Physics of Semiconductor Devices*, 3rd ed.; John Wiley & Sons: Hoboken, NJ, USA, 2006.
28. Wenner, F. A Method of Measuring Earth Resistivity. *Bull. Bur. Stand.* **1915**, *12*, 469–478. [CrossRef]
29. Valdes, L.B. Resistivity Measurements on Germanium for Transistors. *Proc. IRE* **1954**, *42*, 420–427. [CrossRef]
30. Michael, D.K. I-V Software (c). Available online: http://www.kelzenberg.net/software/IV (accessed on 3 March 2023).
31. Ossila Four-Point Probe System. Available online: https://tinyurl.com/y6xttjwl (accessed on 5 March 2023).
32. Eargle, J.M. Resistance Change with Temperature for Copper. In *Electroacoustical Reference Data*; Springer: Boston, MA, USA, 1994; pp. 106–107. [CrossRef]
33. Smits, F.M. Measurement of sheet resistivities with the four-point probe. *Bell Syst. Tech. J.* **1958**, *37*, 711–718. [CrossRef]
34. Shiraiwa, T.; Enoki, M. Fatigue crack behavior of thin copper sheet and its application for smart stress-memory patch. *Strength Fract. Complex.* **2011**, *7*, 205–214. [CrossRef]
35. Judelewicz, M.; Künzi, H.U.; Merk, N.; Ilschner, B. Microstructural development during fatigue of copper foils 20–100 μm thick. *Mater. Sci. Eng. A* **1994**, *186*, 135–142. [CrossRef]

36. Meng, B.; Fu, M.W. Size effect on deformation behavior and ductile fracture in microforming of pure copper sheets considering free surface roughening. *Mater. Des.* **2015**, *83*, 400–412. [CrossRef]
37. Law, K.-Y.; Zhao, H. *Surface Wetting Characterization, Contact Angle, and Fundamentals*, 1st ed.; Springer: Cham, Switzerland, 2015; pp. 7–34.
38. Martinez-Urrutia, A.; Fernandez de Arroiabe, P.; Ramirez, M.; Martinez-Agirre, M.; Mounir Bou-Ali, M. Contact angle measurement for LiBr aqueous solutions on different surface materials used in absorption systems. *Int. J. Refrig.* **2018**, *95*, 182–188. [CrossRef]
39. Gadre, K.S.; Alford, T.L. Contact angle measurements for adhesion energy evaluation of silver and copper films on parylene-n and SiO_2 substrates. *J. Appl. Phys.* **2002**, *93*, 919–923. [CrossRef]

Disclaimer/Publisher's Note: The statements, opinions and data contained in all publications are solely those of the individual author(s) and contributor(s) and not of MDPI and/or the editor(s). MDPI and/or the editor(s) disclaim responsibility for any injury to people or property resulting from any ideas, methods, instructions or products referred to in the content.